


## ORIGINAL RESEARCH

## Remediation and Treatment

# A facile synthesis of bio-inspired hierarchical microstructure TiO<sub>2</sub>: Characterization and photocatalytic activity

Nazli Turkten<sup>1</sup>  | Betul Karatas<sup>1</sup> | Yunus Karatas<sup>1</sup> | Zekiye Cinar<sup>2</sup> | Miray Bekbolet<sup>3</sup>

<sup>1</sup>Department of Chemistry, Kirsehir Ahi Evran University, Kirsehir, Turkey

<sup>2</sup>Department of Chemistry, Yildiz Technical University, Istanbul, Turkey

<sup>3</sup>Institute of Environmental Sciences, Bogazici University, Istanbul, Turkey

## Correspondence

Nazli Turkten, Department of Chemistry, Kirsehir Ahi Evran University, Kirsehir 40100, Turkey.

Email: [nazli.turkten@ahievran.edu.tr](mailto:nazli.turkten@ahievran.edu.tr)

## Funding information

Yildiz Technical University Research Foundation, Grant/Award Number: 2013-01-02-DOP01

## Abstract

Hierarchical photocatalysts have attracted notable concern due to their excellent features such as lower density, higher specific surface area, higher light-harvesting efficiency, and good surface permeability. Generally, such particular properties are achieved via the use of templates, preferentially focusing on natural biological materials. In this respect, rice husk (RH), an environmental waste containing elements C, N, S, and Si was used as a biotemplate to prepare TiO<sub>2</sub> hierarchical microstructure photocatalyst (TiO<sub>2</sub>-HMP) along with TiO<sub>2</sub> nanoparticle photocatalyst (TiO<sub>2</sub>-NP) by a facile sol-gel method. RH and the prepared TiO<sub>2</sub> photocatalysts were characterized by using Fourier transform infrared (FTIR), X-ray powder diffraction (XRD), environmental scanning electron microscope-energy dispersive X-ray analysis (ESEM-EDAX), X-ray photoelectron spectroscopy (XPS), UV-visible diffuse reflectance spectroscopy (UV-DRS), photoluminescence (PL), and Brunauer-Emmett-Teller (BET) methods. The combination of RH and TiO<sub>2</sub> via biotemplate strategy not only altered the band gap ( $E_{bg} = 2.74$  eV) also slightly increased the surface area (~10%). The photocatalytic activities of TiO<sub>2</sub>-NP and TiO<sub>2</sub>-HMP specimens were determined by degradation of 4-nitrophenol (4-NPh) under UV-A light irradiation. TiO<sub>2</sub>-HMP exhibited enhanced photocatalytic activity (≥10%) compared to TiO<sub>2</sub>-NP most probably due to RH originated in-situ self-codoping by the presence of multidopant ions (C, N, S, and Si ions) as verified by EDAX elemental weight distribution profiles. These results demonstrated a beneficial use of an environmental waste in photocatalytic applications.

## KEYWORDS

biotemplate, photocatalysis, rice husk, sol-gel, TiO<sub>2</sub> hierarchical microstructures

## 1 | INTRODUCTION

For decades, many researchers have focused on the application of photocatalysis for degradation of pollutants from water.<sup>1-7</sup> In principle, upon irradiation electron/hole pairs ( $e^-/h^+$ ) are generated and these surface charge carriers further react through subsequent pathways to form reactive oxygen species mainly hydroxyl radicals (HO•), which are responsible for the photocatalytic degradation of the

specified substrates.<sup>1,4,8</sup> TiO<sub>2</sub> is a well-known photocatalyst due to its high photostability, water insolubility, and inexpensiveness. TiO<sub>2</sub> has limited activity under visible light irradiation owing to its broadband gap energy ( $E_{bg}$ ). Doping with various anions and/or metal ions is the most common approach to reduce the  $E_{bg}$  of TiO<sub>2</sub> leading to successful utilization of solar energy.<sup>6,9-19</sup>

Morphological and structural factors intensely affect the photocatalytic activity of TiO<sub>2</sub>, therefore the preparation of different shaped

TiO<sub>2</sub> nanostructures like nanowires, nanotubes, or nanorods has gained more importance. Thus, prepared TiO<sub>2</sub> specimens exhibit superior dispersibility, enhanced porosity, and extended specific surface areas as compared to TiO<sub>2</sub> nanoparticles.<sup>20–22</sup> Besides simply as nanoparticles, various TiO<sub>2</sub> hierarchical photocatalysts have also been constructed in the shape-tailored forms, for example, as nanorods, or nanosheets, to improve photocatalytic activity.<sup>23,24</sup> These hierarchical photocatalysts have attracted much interest due to their excellent features such as higher surface to volume ratio, higher light-harvesting efficiency, ease of removal, high specific surface area, and good surface permeability.<sup>23,25,26</sup> Templates are commonly used in the synthesis and development of these extraordinary morphologies.<sup>27–33</sup> Hard-templating method is the most popular one to synthesize inorganic hierarchical photocatalysts.<sup>34–39</sup> However, the main disadvantage of this method is the removal of the template by chemical etching or calcination processes at elevated temperatures. It is also difficult to achieve a complete removal related to the rupture of the shell.<sup>38,40</sup> Using soft templates such as gas bubbles, microemulsions (e.g., micelles and vesicles), surfactants (e.g., sodium dodecyl sulfate), and droplets is an alternative way to synthesize hierarchical structures.<sup>34,38,41</sup> The removal of soft templates is much easier resulting in a broad range of particle size distribution, irregularities in shape following which shrinkage and deformation occurs via thermal treatment.<sup>42</sup> Biotemplates have been preferred to prepare hierarchical TiO<sub>2</sub> photocatalysts.<sup>43–50</sup> Considerable studies have also been conducted utilizing Gram-positive bacterium (*Staphylococcus aureus*),<sup>46</sup> pollen, albumin, yeast,<sup>48,49</sup> corn starch,<sup>50</sup> tobacco mosaic virus,<sup>51</sup> green-leaf,<sup>52</sup> butterfly wings,<sup>53,54</sup> and eggshell membranes<sup>55</sup> as biotemplates.

Rice husk (RH) is a by-product of rice production during milling and considered as an agricultural waste that causes a significant disposal problem. Either burning or dumping of RH in open fields can cause serious environmental pollution and health problems.<sup>56</sup> RH constitutes about 20% of the weight of rice and is mainly composed of cellulose (50%), lignin (25%–30%), silica (15%–20%), and moisture (10%–15%) along with K, Mg, Al, Fe, and so forth. components. Both RH and RHA as an incineration product of RH, could well be utilized as valuable products for various environmental applications, for example, as adsorbents or construction materials. Investigations performed to evaluate agricultural residues such as RH and RHA and to prepare respective TiO<sub>2</sub> photocatalysts are highly notable and important for waste minimization and/or reuse purposes. So far, RH has been used as a silica and/or carbon source to prepare biological hierarchical porous TiO<sub>2</sub> photocatalysts.<sup>57–67</sup>

The major aim of this study was to use RH as a biotemplate in the synthesis of TiO<sub>2</sub> hierarchical microstructure photocatalyst (TiO<sub>2</sub>-HMP), thereby obtaining a specific route to reduce environmental pollution challenges by utilizing this agricultural waste. More significantly, due to the presence of non-metallic elements (e.g., C, N, S, Si) in RH, TiO<sub>2</sub>-HMP was expected to be self-doped during calcination, leading to enhancement of light absorption. For this purpose, TiO<sub>2</sub>-HMP and TiO<sub>2</sub> nanoparticle photocatalyst (TiO<sub>2</sub>-NP) specimens were synthesized via a modified sol–gel method. Following physico-chemical and morphological characterization, the photocatalysts were subsequently

subjected to activity assessment. 4-NPh displaying toxic, anthropogenic, inhibitory, and refractory properties was selected as a representative model compound of substituted aromatics, which could be present in a range of industrial effluents.

## 2 | MATERIALS AND METHODS

### 2.1 | Materials

Raw RH was obtained from Kastamonu region of North Anatolia-Turkiye. Prior to use, RH was ground and sieved (mesh size = 32 μm), washed with distilled water, and dried at 105°C for 24 h. RH exhibited Brunauer–Emmett–Teller (BET) surface area, pore size, and pore volume as 24.2 m<sup>2</sup>/g, 1.2 nm (microporous), and 0.026 cm<sup>3</sup>/g, respectively (SM, Part 1, FIGURE SM1). Titanium(IV) isopropoxide (TIP) was purchased from Aldrich. Absolute ethanol, glacial acetic acid, and 4-NPh were obtained from Merck. Distilled water (conductivity = 2 μS/cm at 25°C) was used.

### 2.2 | Synthesis of TiO<sub>2</sub> photocatalysts

The TiO<sub>2</sub>-NP was synthesized using TIP/absolute ethanol/glacial acetic acid sol according to the previously described method.<sup>7</sup> For assessment of anatase/rutile phase transition, TiO<sub>2</sub>-NP specimens were calcined at 350, 500, and 600°C for 5 h. TiO<sub>2</sub>-HMP was prepared using a modified sol–gel method. Briefly, 2 g of RH was suspended in distilled water for 2 h, prior to addition into TiO<sub>2</sub> sol that was further stirred overnight at room temperature (25 ± 2°C) and subsequently, kept in dark for 48 h for aging. TiO<sub>2</sub>-HMP was washed with distilled water several times till neutral pH was achieved. Finally, TiO<sub>2</sub>-HMP white precipitate was dried at 105°C for 24 h and calcined at 500°C for 5 h.

### 2.3 | Characterization techniques

The properties of TiO<sub>2</sub>-NP and TiO<sub>2</sub>-HMP specimens were assessed according to the well described characterization methodologies. Since RH was used as a biotemplate, the structural, morphological, and crystal properties of thus formed RHA at 500°C (RHA-500) were also investigated. For comparison purposes, the effects of different calcination temperatures, that is, 350°C (RHA-350) and 600°C (RHA-600) for 5 h were also considered. Fourier transform infrared (FTIR) spectra were performed by using a Perkin Elmer Spectrum One spectrometer with an attenuated total reflectance attachment. All FTIR spectra were recorded in the wavenumber range of 4000–200 cm<sup>-1</sup> and a total of 32 scans were taken with a resolution of 2 cm<sup>-1</sup> at 25°C. The X-ray powder diffraction (XRD) patterns were recorded on a Rigaku-D/MAX-Ultima diffraction spectroscopy using Cu Kα radiation (λ = 1.5418 Å) with an accelerating voltage and emission current as 40 kV and 40 mA, respectively. Environmental Scanning Electron Microscope with Field Emission Gun Equipped with Energy Dispersive

X-ray Analysis Unit (ESEM-FEG/EDAX PhilipsXL-30) instrument was used for the examination of the morphologies. X-ray photoelectron spectroscopy (XPS) measurements were acquired by using a Thermo Scientific K-Alpha X-ray Photoelectron Spectrometer equipped with a hemispherical electron analyzer and an Al-K $\alpha$  micro-focused monochromator. A Perkin Elmer Lambda 35 spectrometer was used to obtain the UV-visible diffuse reflectance spectra (UV-DRS). The photoluminescence (PL) spectra were recorded on an Edinburgh Instruments FS5 spectrofluorometer with an excitation wavelength at  $\lambda = 325$  nm. Thermogravimetry (TG) and differential thermal analyses (DTA) were performed on an EXSTAR TG/DTA 6300 Thermal Analyzer with a heating rate of 10 K/min under nitrogen atmosphere. Nitrogen adsorption/desorption data were recorded by a Quantochrome Nova 2200e Analyzer. Specific surface area and pore sizes were obtained by multi-point BET and BJH methods, respectively. Zeta potential measurements were taken using a Malvern Zetasizer Nano ZS instrument.

## 2.4 | Photocatalytic activity assessment

A double-jacket Pyrex photoreactor connected with a water bath ( $25 \pm 2^\circ\text{C}$ ) equipped with  $5 \times 8$  W blacklight fluorescent lamps ( $\lambda_{\text{max}} = 365$  nm) was utilized. The total photonic fluence was determined as  $3.1 \times 10^{-7}$  Einstein/s by using a potassium ferrioxalate actinometer.<sup>68</sup> Either TiO<sub>2</sub>-NP or TiO<sub>2</sub>-HMP specimens were suspended in 600 ml of 4-NPh solution ( $1.0 \times 10^{-4}$  mol/L) in an ultrasonic bath for 30 min in dark to provide complete dispersion. During irradiation, the suspension was stirred by a mechanical stirrer. Time dependent sampling (10 ml) was performed, and immediate membrane filtration (0.45  $\mu\text{m}$ , Millipore HA) was applied to separate photocatalyst particles from reaction medium to avoid post adsorption via sedimentation. Photocatalytic degradation of 4-NPh was monitored by absorbance recordings at  $\lambda_{\text{max}} = 318$  nm using an Agilent 8453 UV-Visible spectrophotometer. The molar extinction coefficient of 4-NPh was determined as  $\epsilon = 9249$  L/mol cm.

## 3 | RESULTS AND DISCUSSION

### 3.1 | Structural and morphological properties of RH and RHA

#### 3.1.1 | FTIR analysis of RH and RHA

The FTIR provided information related to the functional groups of both organic and inorganic parts of RH. Organic part of RH was typically composed of lignocellulosic material, while the inorganic part was mostly silica originating from the outer epidermal cells. The rest of the inorganic part included elements such as Mg, Al, and Fe.<sup>69</sup> Due to the applied different calcination temperatures, possible alterations on the surface functional groups of RHA were also monitored. The FTIR spectrum of RH (Figure 1) expressed a wide band in the range of 3600–3000  $\text{cm}^{-1}$  with a maximum at 3326  $\text{cm}^{-1}$  related to the

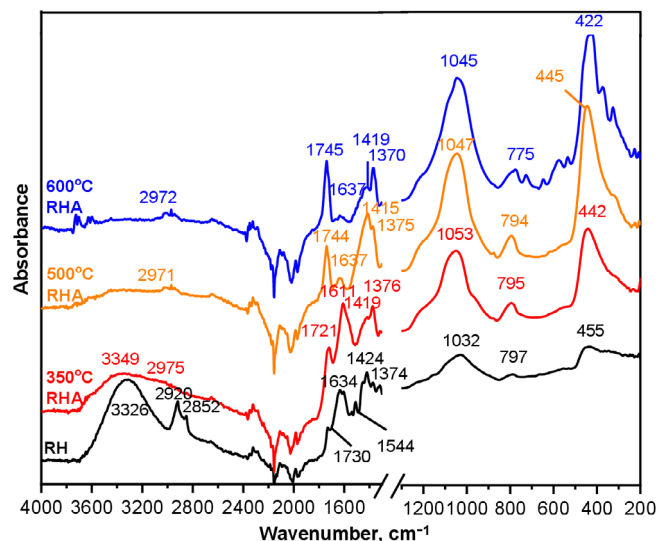


**FIGURE 1** Fourier transform infrared (FTIR) spectra of rice husk (RH) and RHA-350, RHA-500 and RHA-600.

stretching vibration of intermolecular hydrogen bonded —OH groups in lignocellulosic structures and the stretching vibrations of —OH bonds in adsorbed water.<sup>70,71</sup> The low intensity bands at 2920 and 2852  $\text{cm}^{-1}$  could be attributed to the C—H stretching bonds of the —CH<sub>3</sub> and —CH<sub>2</sub> groups, respectively.<sup>72</sup> The weak band at 1730  $\text{cm}^{-1}$  was assigned to C=O stretching modes of aldehyde groups of hemicellulose.<sup>59</sup> The medium band at 1634  $\text{cm}^{-1}$  corresponded to the bending vibration of water trapped in the silica matrix or C=C stretching vibration.<sup>61</sup> The absorption band at 1424  $\text{cm}^{-1}$  was related to CH<sub>2</sub> scissoring motion in cellulose or asymmetric bending in CH<sub>3</sub> in lignin, while the band at 1544  $\text{cm}^{-1}$  was ascribed to aromatic skeleton C—C stretching in lignin.<sup>73</sup> The weak band at 1374  $\text{cm}^{-1}$  represented the aromatic C—H bending vibration in cellulose and hemicellulose or carboxyl carbonate.<sup>73,74</sup> The region of the spectrum 1148–960  $\text{cm}^{-1}$  consisted of the superposition of vibrations of the C—OH and Si—O bonds in the siloxane groups located at 1032  $\text{cm}^{-1}$  in RH. The two bands at 797 and 455  $\text{cm}^{-1}$  were related to symmetric vibrations of the Si—O bonds in the silicon oxygen tetrahedrons (SiO<sub>4</sub>) and Si—O—Si bending vibrations, respectively.<sup>59,75,76</sup>

The FTIR spectra of RHA specimens displayed that the O—H stretching and HO—H band at  $\sim 3326$   $\text{cm}^{-1}$  was almost negligible in RHA-500 and was completely removed in RHA-600 (Figure 1). This result indicated the expected decrease of surface hydroxyl groups as the calcination temperature increased.<sup>77</sup> The stretching bands at 2852  $\text{cm}^{-1}$  (C—H) and 1544  $\text{cm}^{-1}$  (C—C) disappeared in RHA-350, while the intensities of the bands at 2920  $\text{cm}^{-1}$  (C—H) and 1424  $\text{cm}^{-1}$  (CH<sub>2</sub> and CH<sub>3</sub> vibrations) decreased as related to the decomposition of organic parts. The intensities of absorption bands observed at 1730  $\text{cm}^{-1}$  (C=O stretching), 1634  $\text{cm}^{-1}$  (C=C or bending water vibrations), and 1374  $\text{cm}^{-1}$  (aromatic C—H bending or carboxyl carbonate) in the RH spectrum increased in RHA-350 due to the partial decomposition of cellulose.<sup>78</sup> The band related to the functional group of C=O gradually increased with increasing calcination temperature and shifted to a higher wavenumber. However, the intensity of

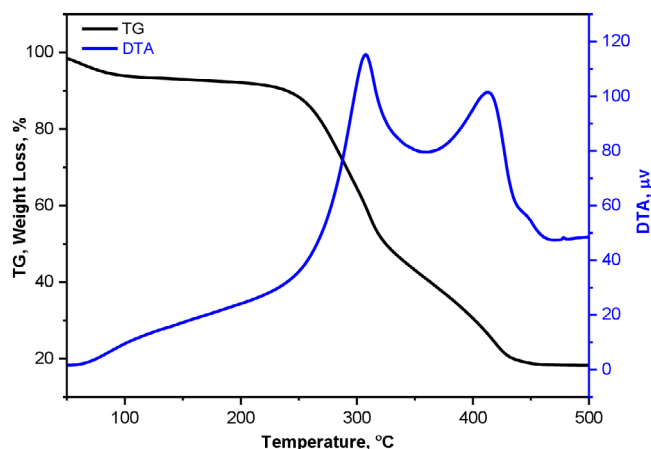


**FIGURE 2** Thermogravimetry (TG) and differential thermal analyses (DTA) curves of rice husk (RH).

the band at  $1611\text{ cm}^{-1}$  in RHA-350 decreased as the calcination temperature increased to 500 and  $600^\circ\text{C}$ . The band at  $1419\text{ cm}^{-1}$  was increased in RHA-350 spectrum, then decreased upon calcination at higher temperatures. An opposite trend was observed for the band at  $1376\text{ cm}^{-1}$ . Heating RH at  $500^\circ\text{C}$  have resulted in thermal decomposition of both cellulose and lignin.<sup>78</sup> Upon calcination, intensity enhancement of the characteristic silica bands at  $1032$ ,  $797$ , and  $455\text{ cm}^{-1}$  were noticed most probably due to the generation of new siloxane groups as a result of the thermal decomposition of the organic parts.<sup>77</sup>

### 3.1.2 | Thermal properties and TG/DTA analysis of RH

In order to clarify the observed alterations in the FTIR spectra of RH, thermal analysis was performed. TG and DTA curves revealed three distinct stages of weight loss (Figure 2). The first stage with 6% weight loss and an endothermic peak at around  $100^\circ\text{C}$  was attributed to the dehydration of adsorbed water. It was followed by a drastic weight loss of around 50% with a broad exothermic peak in the temperature range of  $240\text{--}360^\circ\text{C}$  centered at  $307^\circ\text{C}$ . This stage could be ascribed to the thermal decomposition of cellulose and hemicellulose with the weight loss due to the oxidation of carbon forming volatile components, tar, and char. The third stage, with a weight loss of 20% related to an exothermic peak in the temperature range of  $360\text{--}450^\circ\text{C}$  centered at  $412^\circ\text{C}$  indicated the thermal decomposition of lignin.<sup>79,80</sup> The total weight loss (>80%) was in good agreement with the literature findings that RH contains nearly 20% silica and a high amount of carbon<sup>81</sup> as supported by the FTIR spectral features indicating that lignin was thermally more stable than cellulose and hemicellulose.

### 3.1.3 | XRD analysis of RH and RHA

The XRD spectroscopic profiles were presented in Figure 3. The diffractogram of the RH showed a wide peak in  $19^\circ\text{--}30^\circ$  centered at

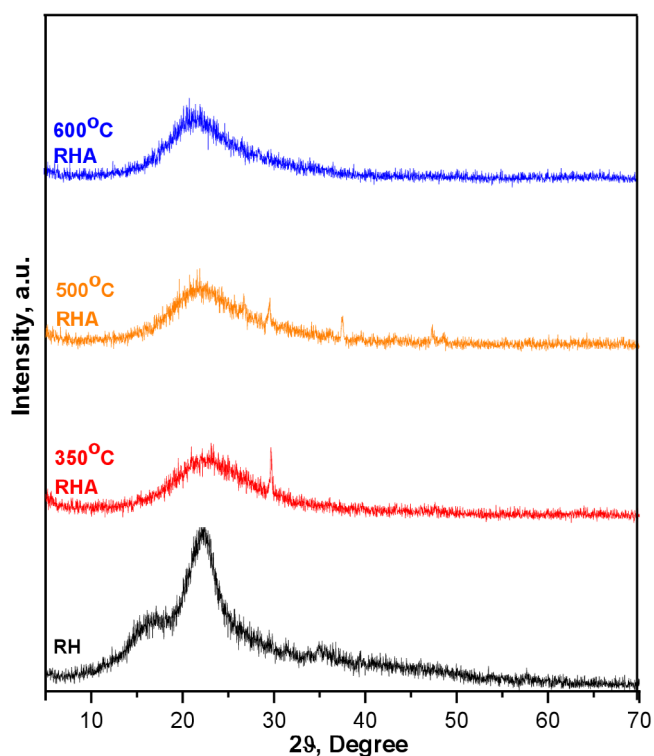


**FIGURE 3** X-ray powder diffraction (XRD) diffractograms of rice husk (RH) and RHA-350, RHA-500 and RHA-600.

around  $22^\circ$ , which was ascribed to the characteristics of amorphous silica. The peak at  $17^\circ$  was attributed to the remnant carbon matrix.<sup>59</sup> As the temperature increased to  $350^\circ\text{C}$ , and higher temperatures, the amorphous  $\text{SiO}_2$  peak shifted to a lower angle and broadened, while the peak at  $17^\circ$  disappeared. These changes could be explained to an increment in the structural order of the amorphous  $\text{SiO}_2$  toward the cristobalite phase thus causing the densification of the structure.<sup>82</sup> This result was consistent with the FTIR results indicating the presence of silica in both the RH and RHA structures.

### 3.1.4 | Morphology and ESEM analysis of RH and RHA

The ESEM micrographs were presented in Figures 4 and 5. The outer surface of RH resembled a corn cob like and a lamellar structure consisting of thin tubes (Figure 4). The micrograph RHA-350 expressed the main skeleton with some minor morphological deformations. A general breakdown of the RH skeleton into smaller and more irregular-shaped fragments occurred as the calcination temperature reached up to  $500^\circ\text{C}$ . The morphology of RHA-500 was quite similar to that of RHA-600.<sup>83</sup> The inner surface of the RH and RHA samples were illustrated in Figure 5. ESEM micrograph of RH was composed of a fibrous structure with thin hairs. As the temperature was increased, the fibers became thinner and an increase in void volume expressing a spongy structure could be visualized. These changes on the surface resulted in the formation of bumps and micro pores due



**FIGURE 4** Outer surface environmental scanning electron microscope (ESEM) images of rice husk (RH) and RHA-350, RHA-500 and RHA-600.

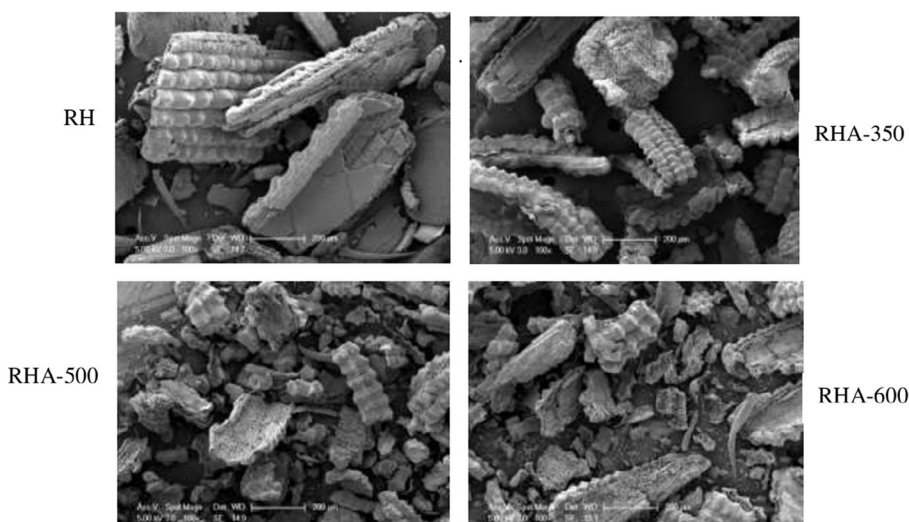
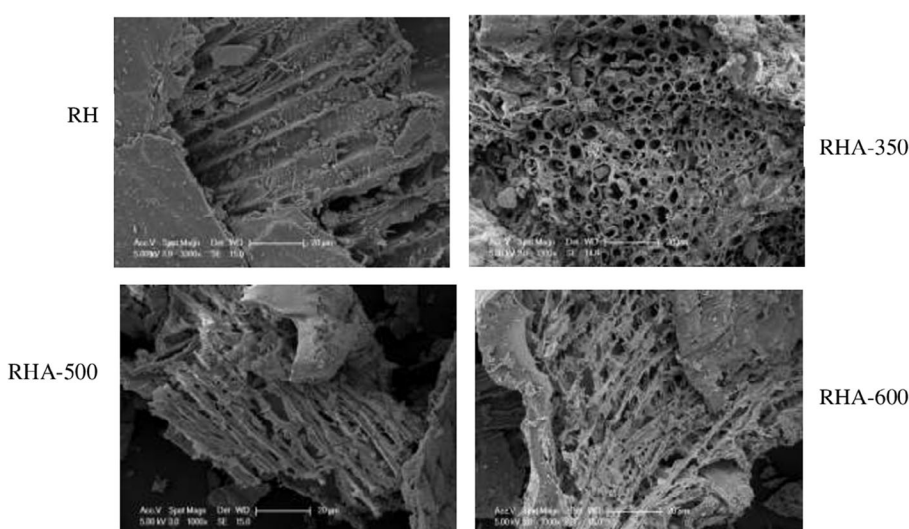


**FIGURE 5** Inner surface environmental scanning electron microscope (ESEM) images of rice husk (RH) and RHA-350, RHA-500 and RHA-600.



to thermal decomposition.<sup>84</sup> EDAX elemental weight distribution of RH and RHA samples were presented in SM, Part 2, FIGURE SM2. The chemical composition of RH was mainly Si and O atoms along with minor amounts of C, N, S, Ca, and Mg. This information was also verified by XPS spectrum of RH and related information was presented in SM, Part 3, FIGURE SM3.

### 3.2 | Structural, morphological, and optical properties of TiO<sub>2</sub>-NP and TiO<sub>2</sub>-HMP specimens

Characterization of photocatalysts was performed according to the well described techniques presented in the methodology section.<sup>85</sup>

#### 3.2.1 | Crystallinity and XRD analysis of TiO<sub>2</sub>-NP and TiO<sub>2</sub>-HMP

Figure 6 displayed the XRD diffractograms of the TiO<sub>2</sub>-NP specimens in the range of 2°–70° based on MDI-JADE6 library. The

TiO<sub>2</sub>-NP specimens calcined at 350, 500, and 600°C for 5 h represented the effect of calcination temperature on crystallite phases. The diffractogram of TiO<sub>2</sub> calcined at 350°C contained only anatase peaks, indicating the sole presence of anatase phase. The emergence of rutile phase along with anatase phase was evidenced upon calcination at 500 and 600°C. The fractional phase content of TiO<sub>2</sub> specimens could be calculated by using the below given Equations (1) and (2) where A and R denoted anatase and rutile, respectively.

$$A = K_A I_A / (K_A I_A + K_R I_R) \quad (1)$$

$$R = K_R I_R / (K_A I_A + K_R I_R) \quad (2)$$

Where,  $I_A$  (0 1 1) and  $I_R$  (1 1 0) were the integrated intensities of the main peaks ascribed to anatase and rutile, respectively and  $K_A = 0.886$  and  $K_R = 1$ .<sup>86,87</sup> Upon use of the Equations (1) and (2), TiO<sub>2</sub>-NP calcined at 500°C was found to be composed of 87% anatase and 13% rutile phases signifying a close similarity to commercial TiO<sub>2</sub> P25.<sup>88</sup> Further increase in calcination temperature to 600°C

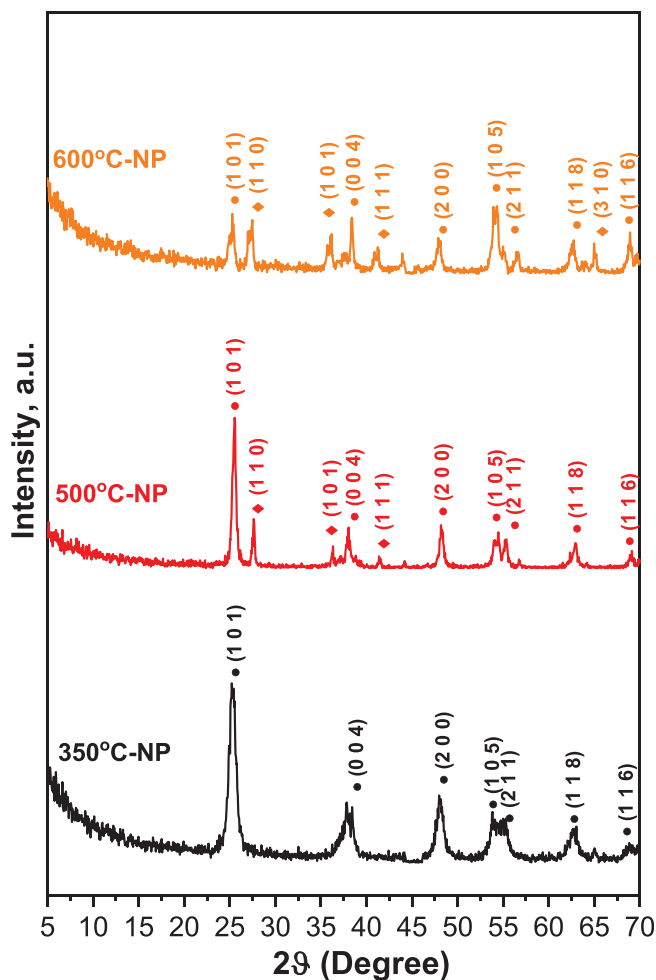


**FIGURE 6** Calcination temperature effect on the X-ray powder diffraction (XRD) diffractograms of  $\text{TiO}_2$  nanoparticle photocatalyst ( $\text{TiO}_2$ -NP) specimens (• anatase, ♦ rutile).

promoted transition from anatase phase to rutile phase composition resulting in almost equal proportions.

The effect of the calcination period on the  $\text{TiO}_2$ -NP crystallinity was also elucidated via XRD diffractograms (SM, Part 4, FIGURE SM4). The calcination temperature was kept constant at  $500^\circ\text{C}$  as the calcination period varied from 1 to 5 h. After one-hour of calcination, only anatase diffraction peak (1 0 1) was observed. Upon incremental increase in calcination period from 3 to 5 h, a transition from anatase to rutile phase was expected as evidenced by emergence of rutile peaks located at (1 1 0).

The XRD diffractograms of  $\text{TiO}_2$ -NP and  $\text{TiO}_2$ -HMP specimens calcined at  $500^\circ\text{C}$  for 5 h were comparatively presented in Figure 7. Diffractogram of  $\text{TiO}_2$ -NP displayed an intense peak at  $25.53^\circ$  related to the characteristic anatase (1 0 1) phase, whereas the characteristic rutile (1 1 0) peak was observed at  $25.70^\circ$ . The peaks at  $37.92^\circ$ ,  $48.25^\circ$ ,  $54.21^\circ$ ,  $55.29^\circ$ ,  $62.89^\circ$ , and  $69.26^\circ$  corresponded to (0 0 4), (2 0 0), (1 0 5), (2 1 1), (1 1 8), and (1 1 6) planes of anatase and the ones at  $36.27^\circ$  and  $41.29^\circ$  corresponded to (1 0 1) and (1 1 1) planes of rutile, respectively. Diffractogram of  $\text{TiO}_2$ -HMP displayed anatase diffraction peaks

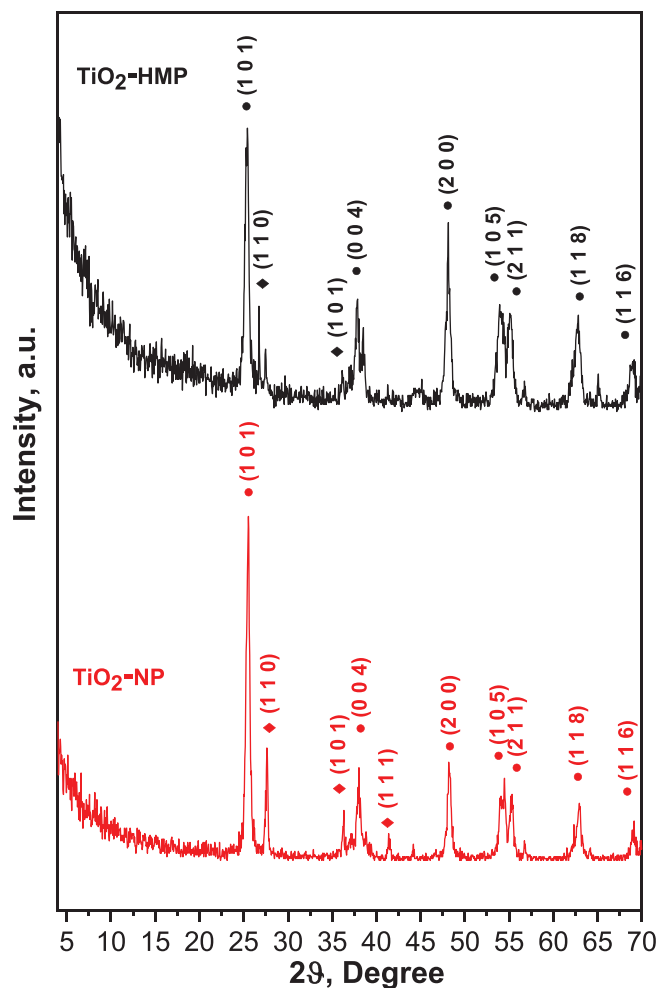


**FIGURE 7** X-ray powder diffraction (XRD) diffractograms of  $\text{TiO}_2$  nanoparticle photocatalyst ( $\text{TiO}_2$ -NP) and  $\text{TiO}_2$  hierarchical microstructure photocatalyst ( $\text{TiO}_2$ -HMP) specimens calcined at  $500^\circ\text{C}$  for 5 h (• anatase, ♦ rutile).

shifted to lower angles as  $25.47^\circ$ ,  $37.81^\circ$ ,  $48.14^\circ$ ,  $53.98^\circ$ ,  $55.15^\circ$ ,  $62.78^\circ$ , and  $69.08^\circ$ , respectively. These slight shifts to lower angles could be attributed to the presence of RH originated ions, that is, C, N, S, and Si. The characteristic diffraction peak of amorphous  $\text{SiO}_2$  ( $\sim 22^\circ$ ) was hardly observed, which indicated that the related minor RH peak was hindered by the highly intense signals of the crystalline  $\text{TiO}_2$  diffraction peaks. The absence of a diffraction peak at  $\sim 31^\circ$  revealed that the two specimens were devoid of brookite structure. Based on the (1 0 1) anatase diffraction planes, crystallite size ( $D$ ) could be calculated by using the Scherrer equation (Equation 3);

$$D = (K\lambda) / (\beta \cos\theta) \quad (3)$$

$K = 0.9$ ,  $\lambda = 1.5418 \text{ \AA}$  for  $\text{Cu K}\alpha$ ,  $\theta =$  Bragg angle and  $\beta =$  full width at half maximum intensity (FWHM, radians).<sup>89</sup> The crystallite sizes were calculated as 33.1, and 16.6 nm for  $\text{TiO}_2$ -NP and  $\text{TiO}_2$ -HMP, respectively. This finding indicated that the use of RH biotemplate caused a decrease in the crystallite size of  $\text{TiO}_2$ -NP in

accordance with the broadening of the diffraction peaks. The lattice parameters were calculated and presented in SM, Part 4.

### 3.2.2 | FTIR analysis of TiO<sub>2</sub>-NP and TiO<sub>2</sub>-HMP

The FTIR spectra of TiO<sub>2</sub>-NP and TiO<sub>2</sub>-HMP specimens were presented in Figure 8. The low bands at 1633 and 1642 cm<sup>-1</sup> were assigned to the bending mode of adsorbed water molecules for TiO<sub>2</sub>-NP and TiO<sub>2</sub>-HMP

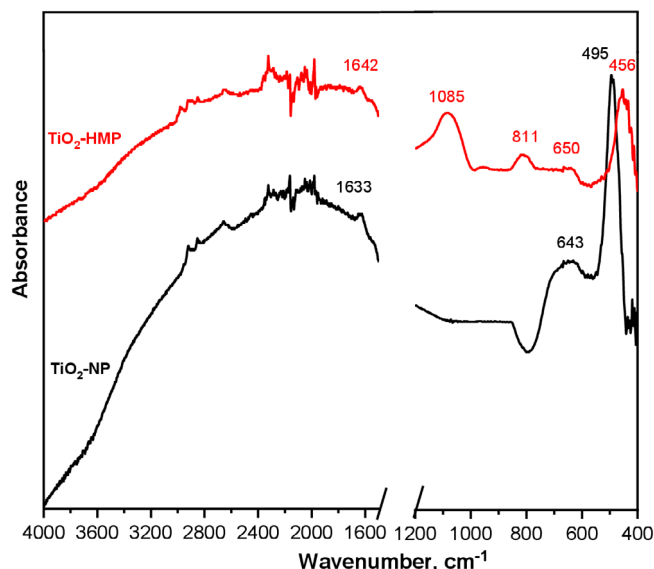


**FIGURE 8** Fourier transform infrared (FTIR) spectra of TiO<sub>2</sub> nanoparticle photocatalyst (TiO<sub>2</sub>-NP) and TiO<sub>2</sub> hierarchical microstructure photocatalyst (TiO<sub>2</sub>-HMP) specimens.

specimens, respectively. In the spectral region below 972 cm<sup>-1</sup> various characteristic bands related to Ti–O stretching and O–Ti–O bending vibrations were noticed.<sup>90</sup> The spectrum of TiO<sub>2</sub>-HMP exhibited three more peaks at 1085, 811, and 456 cm<sup>-1</sup> most probably originating from the RH biotemplate. The band at 1085 cm<sup>-1</sup> was assigned to the C–OH and Si–O bonds in the siloxane groups. The bands located at 811 and 456 cm<sup>-1</sup> corresponded to the symmetric vibrations of Si–O bonds and bending vibrations of Si–O–Si, respectively<sup>59,75,76</sup> indicating that the TiO<sub>2</sub> coating process over RH was successfully achieved.

### 3.2.3 | Morphology and ESEM with EDAX analysis TiO<sub>2</sub>-NP and TiO<sub>2</sub>-HMP

The ESEM micrograph of TiO<sub>2</sub>-NP expressed the presence of various polyhedral shaped particles with slight agglomerations (Figure 9a). The EDAX spectrum appointed Ti and O as the principal components as expected. The TiO<sub>2</sub>-HMP particles were larger, elongated with sharp edges, and expressed rough surfaces compared to TiO<sub>2</sub>-NP (Figure 9b). The observed cracks were most probably due to the removal of RH and breaking down of the organic species retaining the original hierarchical RH structure.<sup>60</sup> ESEM micrographs with different magnifications and EDAX elemental weight distribution profiles of TiO<sub>2</sub>-NP and TiO<sub>2</sub>-HMP specimens were presented in SM, Part 5, FIGURE SM5-SM6.

### 3.2.4 | XPS analysis of TiO<sub>2</sub>-NP and TiO<sub>2</sub>-HMP

The XPS spectra exhibited two main regions related to Ti 2p at ~460 eV and O 1s at ~530 eV for both specimens, while four regions

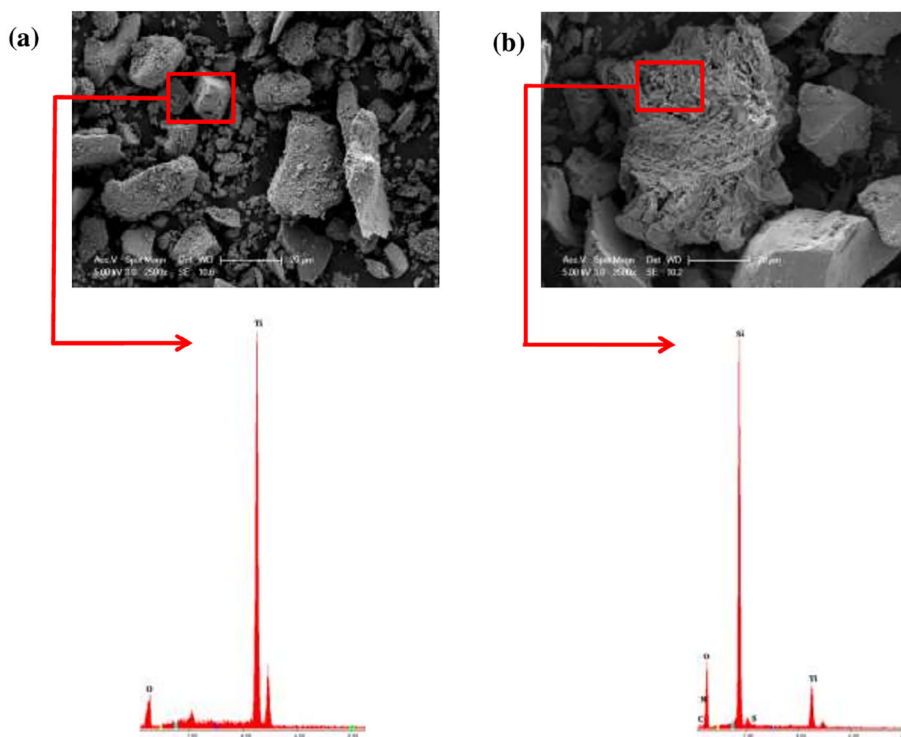


**FIGURE 9** Environmental scanning electron microscope-energy dispersive X-ray analysis (ESEM-EDAX) micrographs of (a) TiO<sub>2</sub> nanoparticle photocatalyst (TiO<sub>2</sub>-NP) (b) TiO<sub>2</sub> hierarchical microstructure photocatalyst (TiO<sub>2</sub>-HMP) specimens.

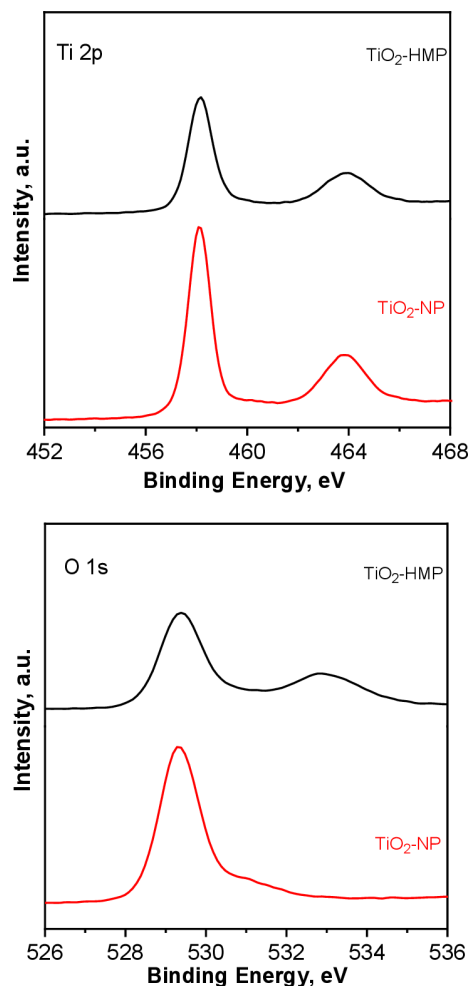


**FIGURE 10** Ti 2p and O 1s core levels of TiO<sub>2</sub> nanoparticle photocatalyst (TiO<sub>2</sub>-NP) and TiO<sub>2</sub> hierarchical microstructure photocatalyst (TiO<sub>2</sub>-HMP) specimens.

belonged to N 1s at ~400 eV, C 1s at ~283 eV, S 2p at ~155 eV and Si 2p at ~103 eV for TiO<sub>2</sub>-HMP specimens (Figures 10 and 11). The presence of Ti, O, Si, C, S, and N elements in the TiO<sub>2</sub>-HMP spectrum confirmed the presence of both TiO<sub>2</sub> and RH components. Other elements such as Ca, K, and Mg were not detected as demonstrated by ESEM-EDAX distribution in RH (SM, Part 2, FIGURE SM2). High resolution XPS spectrum of TiO<sub>2</sub>-NP consisted of two binding energy peaks at 458.1 and 463.9 eV corresponding to the Ti 2p<sub>1/2</sub> and Ti 2p<sub>3/2</sub> lines, respectively (Figure 10). This result confirmed that the oxidation state of Ti was IV.<sup>91,92</sup> Ti 2p binding energies of TiO<sub>2</sub>-HMP (at 458.2 and 464.0 eV) shifted slightly to higher binding energies with regard to TiO<sub>2</sub>-NP indicating the presence and coordination of C, N, S, and Si ions originating from RH. Xu and Zeng reported that the electronegativity difference between Si (1.8) and Ti (1.5) could cause a higher binding energy. This shift could indicate an interaction between TiO<sub>2</sub> and SiO<sub>2</sub> resulting in a Ti—O—Si bond formation.<sup>93</sup> The higher electronegativity of S (2.5) could lead to a decrease in the electron density around Ti resulting in an increase in the binding energy.<sup>94</sup> Conversely, the electronegativity of N and C was lower than that

of O, which could also cause increased electron density on Ti.<sup>95,96</sup> The existence of different electronegative ions could influence the electron density on Ti and could hardly change the binding energy of Ti 2p. The O 1s spectrum of TiO<sub>2</sub>-NP revealed a major peak at 529.3 eV corresponding to the crystal lattice oxygen (O<sub>2</sub><sup>-</sup>) and a small peak located at 530.7 eV was attributed to the surface hydroxyl groups species.<sup>21</sup> For the O 1s core level spectrum of TiO<sub>2</sub>-HMP, the main peak at 529.4 eV was practically similar to TiO<sub>2</sub>-NP, which was assigned to the crystal lattice oxygen (O<sub>2</sub><sup>-</sup>). The second peak at 532.7 eV was related to the Si—O bond in SiO<sub>2</sub> structure derived after the calcination of the biotemplate.<sup>21,59</sup>

Introduction of C, N, S, and Si into the structure resulting from the calcination of RH was also detected in XPS spectrum of TiO<sub>2</sub>-HMP specimen (Figure 11) and this finding was compatible with the EDAX (Figure 9b). C 1s core level spectrum was consisted of two peaks that were mostly found in lignocellulosic materials, that is, cellulose and biomass wastes. The first peak at 284.4 eV was assigned to C sp<sup>2</sup> graphitic carbon, while the other peak at 286.4 eV was related to C—O, C—H bonds in phenolic, alkoxy, and ether groups, respectively.<sup>59</sup> N 1s peaks were located at 400.6 and 403.5 eV related to Ti—N—O, surface-adsorbed nitrogen species, respectively.<sup>97</sup> The peak at 154.8 eV in the S 2p spectrum in Figure 11 corresponded to S 2p<sub>3/2</sub> electrons of S.<sup>98</sup> Si 2p peak observed at 103.7 eV was ascribed to Si 2p<sub>1/2</sub> electrons.<sup>99</sup> The major effect of calcination could be emphasized as in-situ generated N—S self-codoping of TiO<sub>2</sub>.

### 3.2.5 | Optical absorbance and UV-DRS analysis of TiO<sub>2</sub>-NP and TiO<sub>2</sub>-HMP

The resulting effect of biotemplate use on the optical performance of TiO<sub>2</sub>-NP as TiO<sub>2</sub>-HMP specimens were articulated by UV-DRS spectroscopy (Figure 12). TiO<sub>2</sub>-NP spectrum displayed a distinct absorption edge at ~325 nm rising up to ~410 nm, while TiO<sub>2</sub>-HMP had a high absorption band starting from ~330 nm extending up to ~450 nm. Doping of TiO<sub>2</sub> with nonmetal/halogen elements such as C, N, S, F, and Cl could induce a bathochromic shift in absorption of TiO<sub>2</sub>.<sup>100</sup> The reason of this chromic phenomenon could be attributed to the presence of biotemplate originated self-doped anions, for example, N in the TiO<sub>2</sub> structure<sup>57</sup> as verified by XPS analysis (Figure 11).

The UV-DRS spectra were transformed to Kubelka-Munk function,<sup>101</sup> following which Tauc plot ( $[(F(R) \cdot hv)^n \text{ vs. } hv$  ( $hv = \text{photon energy, eV and } n = 1/2)$ ) was used for the determination of the indirect band gap values of all samples<sup>102</sup> (Figure 12).

Kubelka-Munk is expressed reflectance, R deduced from the UV-DRS spectra (Equation 1)

$$F(R) = \frac{(1-R)^2}{2R} \quad (4)$$

The band gap energies of all the photocatalysts were calculated by assuming that they were indirect semiconductors.<sup>102</sup> The E<sub>bg</sub> and



**FIGURE 11** C 1s, N 2s, S 2p, and Si 2p core levels of TiO<sub>2</sub> hierarchical microstructure photocatalyst (TiO<sub>2</sub>-HMP) specimen.

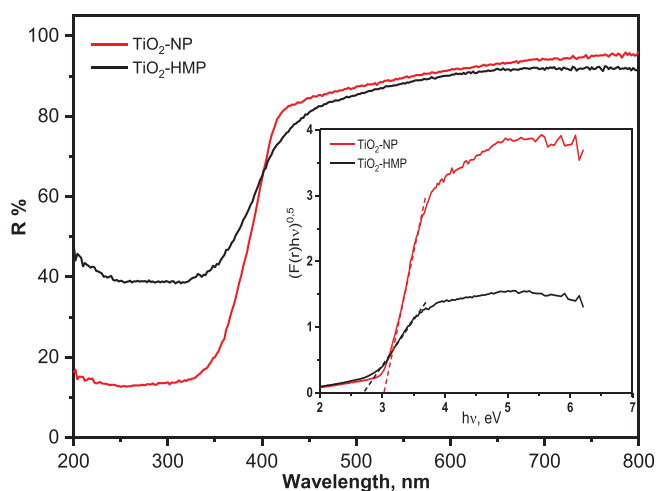
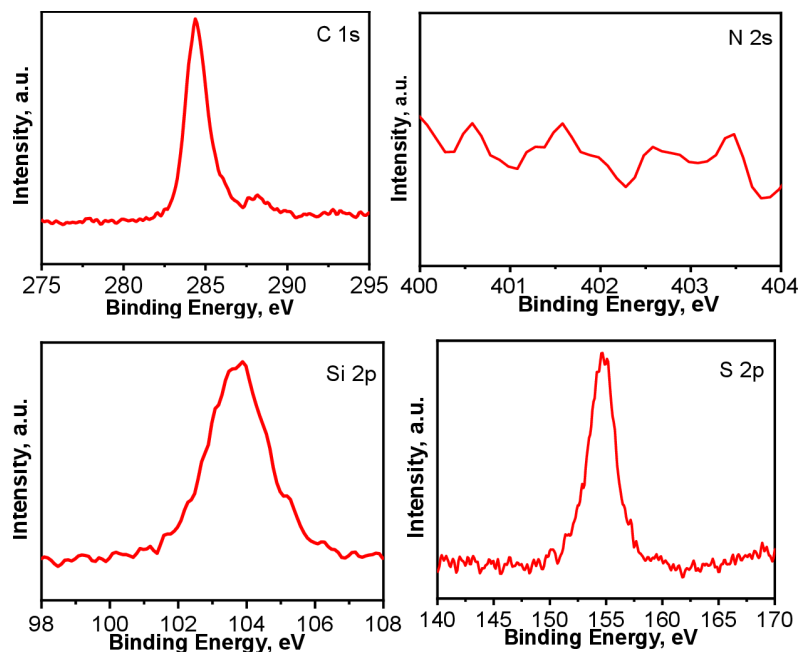


**FIGURE 12** UV-visible diffuse reflectance spectra (UV-DRS) spectra and estimated band gaps (inserted) of TiO<sub>2</sub> nanoparticle photocatalyst (TiO<sub>2</sub>-NP) and TiO<sub>2</sub> hierarchical microstructure photocatalyst (TiO<sub>2</sub>-HMP) specimens.

the corresponding wavelengths were 3.04 eV ( $\lambda = 408$  nm) and 2.74 eV ( $\lambda = 452$  nm) for TiO<sub>2</sub>-NP and TiO<sub>2</sub>-HMP, respectively indicating that the modification of TiO<sub>2</sub> with RH resulted in a reduction in  $E_{bg}$  revealing a red shift.

### 3.2.6 | Photoluminescence analysis of TiO<sub>2</sub>-NP and TiO<sub>2</sub>-HMP

The PL technique has been widely used to examine the recombination of electrons and holes in semiconductors due to the dependency on peak intensity.<sup>85,103,104</sup> PL spectral features of TiO<sub>2</sub>-HMP expressed

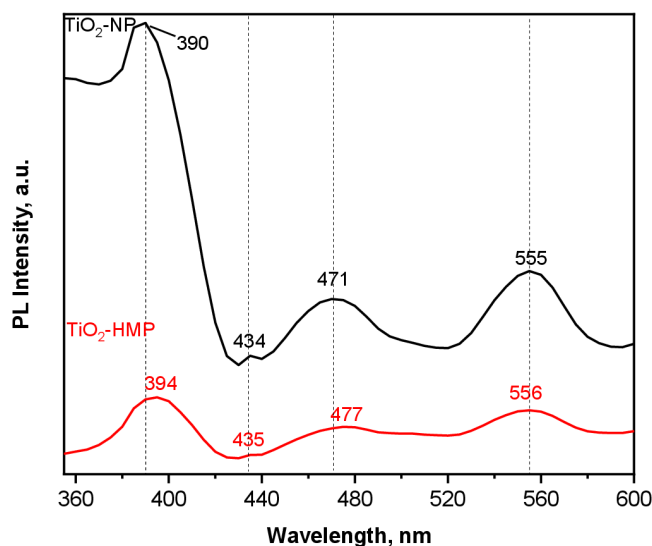


**FIGURE 13** Photoluminescence (PL) spectra of TiO<sub>2</sub> nanoparticle photocatalyst (TiO<sub>2</sub>-NP) and TiO<sub>2</sub> hierarchical microstructure photocatalyst (TiO<sub>2</sub>-HMP) specimens.

close resemblance to TiO<sub>2</sub>-NP spectrum (Figure 13). A sharp UV emission peak at  $\lambda = 390$  nm in TiO<sub>2</sub>-NP PL spectrum could be assigned to the radiative annihilation of excitations of TiO<sub>2</sub> or corresponded to the recombination of free excitons.<sup>105,106</sup> The weak peak at  $\lambda = 434$  nm could be attributed to the self-trapped excitons, whereas the blue-green emission at  $\lambda = 471$  nm and the green emission at  $\lambda = 555$  nm were related to the electrons bound or trapped in oxygen vacancy centers.<sup>107</sup> A red shift was noticed on the emission peaks of TiO<sub>2</sub>-HMP due to the self-assembled multidoped structure of the photocatalyst. The PL intensity profiles of TiO<sub>2</sub>-HMP were altered compared to that of TiO<sub>2</sub>-NP suggesting the

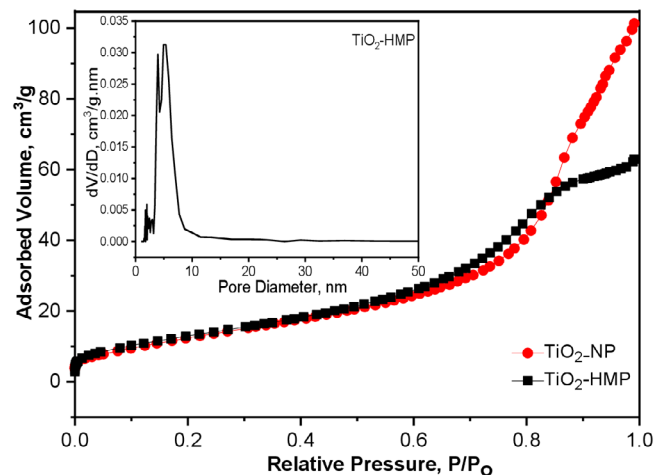


**FIGURE 14** Nitrogen adsorption isotherms of TiO<sub>2</sub> nanoparticle photocatalyst (TiO<sub>2</sub>-NP) and TiO<sub>2</sub> hierarchical microstructure photocatalyst (TiO<sub>2</sub>-HMP) specimens and pore size distribution curve of TiO<sub>2</sub>-HMP (inserted).

suppression of electron–hole recombination by the presence of SiO<sub>2</sub> or multidopant ions (C, N, and S ions). This suppression due to the incorporation of SiO<sub>2</sub> could enhance the photocatalytic activity<sup>103</sup> whereas a retardation effect was also reported due to the low available surface Ti active sites.<sup>104</sup> Besides, the surface defects such as O vacancies and doping impurities could act as trap states generating intermediate energy levels within the band gap and resulting in a lower energy emission.<sup>106</sup> In addition, the earlier PL studies on C, N, and S tri-doped TiO<sub>2</sub> revealed a lowered PL intensity compared to TiO<sub>2</sub> indicating the suppression of photo-generated electron–hole recombination.<sup>108,109</sup> Based on the PL results, an exhibition of a higher photocatalytic activity performance was predicted for the TiO<sub>2</sub>-HMP specimen.

### 3.2.7 | BET analysis

The BET surface area of TiO<sub>2</sub>-NP and TiO<sub>2</sub>-HMP specimens was determined by nitrogen adsorption isotherms (Figure 14). The adsorption curves of both TiO<sub>2</sub>-NP and TiO<sub>2</sub>-HMP expressed a typical Type IV isotherm that the primary region could be ascribed to monolayer-multilayer adsorption.<sup>110</sup> The enhancement at lower relative pressure range ( $0.65 < P/P_0 < 0.85$ ) revealed the presence of pores, and at a high pressure range ( $0.85 < P/P_0 < 1$ ) demonstrated the empty spaces between particles in TiO<sub>2</sub>-HMP.<sup>54</sup> BET surface areas of TiO<sub>2</sub>-NP and TiO<sub>2</sub>-HMP were 50 and 55 m<sup>2</sup>/g, respectively. The slight increase in surface area could be ascribed to the introduction of SiO<sub>2</sub> formed during calcination to the surface area of TiO<sub>2</sub>. Potential effect of the bio-templete type in relation to the applied calcination temperature on the surface area have been reported.<sup>60,111,112</sup> The average pore size of the TiO<sub>2</sub>-HMP specimen was ca. 5 nm implying a microporous character with a narrow distribution exposing similarity to the mesoporous TiO<sub>2</sub>/SiO<sub>2</sub> structure.<sup>111</sup>

**TABLE 1** Kinetic model parameters

First order kinetic model parameters			
	Rate constant $k \times 10^{-3}, \text{min}^{-1}$	Half-life $t_{1/2}, \text{min}$	Rate $R \times 10^{-3}$ , mol/L min
Photocatalyst dose, g/100 ml			
TiO <sub>2</sub> -NP			
0.1	4.10	195	3.55
0.2	7.14	131	5.27
0.3	5.06	160	4.32
0.4	4.60	167	4.14
0.5	1.55	485	1.43
TiO <sub>2</sub> -HMP			
0.1	1.77	392	1.64
0.2	1.93	359	1.79
0.3	2.71	256	2.56
0.4	4.66	149	3.80
0.5	8.22	84	7.64
Initial concentration of 4-NPh, mol/L; TiO <sub>2</sub> HMP 0.5 g/100 ml			
TiO <sub>2</sub> -HMP			
$6.0 \times 10^{-5}$	12.4	56	7.44
$8.0 \times 10^{-5}$	9.52	73	7.62
$1.0 \times 10^{-4}$	8.22	84	7.64
$1.2 \times 10^{-4}$	4.90	141	5.88

### 3.2.8 | Photocatalytic activity

The expected role of photocatalyst loading and initial substrate concentration was investigated along with preliminary experiments revealing the effect of dark interactions and direct photolytic reactions. Removal efficiency was expressed in terms of degradation percentage (Equation 5) calculated as;

$$\text{Degradation efficiency, \%} = (C_0 - C_t / C_0) \times 100 \quad (5)$$

where  $C_0$  and  $C_t$  denoted initial concentration ( $t = 0$ ) and concentration at any irradiation time,  $t$  (min).

Kinetic data were also fitted to first order kinetic model (Equation 6) described as;

$$\text{Rate} = -d[C]/dt = k[C] \quad (6)$$

where  $k$  denoted first order reaction rate constant ( $k$ , time<sup>-1</sup>) revealing rate of reaction as Rate (mol/L time) =  $k \times C_0$  and half-life (time)  $t_{1/2} = 0.693/k$ .

The effect of photocatalyst loading in the range of 0.1–0.6 g/100 ml on the removal efficiency of 4-NPh ( $C_0 = 1.0 \times 10^{-4}$  mol/L) was examined (SM, Part 6, FIGURE SM7). Irradiation time dependent variations pointed out the effect of photocatalyst loading, indicating the optimum dose as 0.2 and 0.5 g/100 ml for TiO<sub>2</sub>-NP and TiO<sub>2</sub>-HMP, respectively. Upon use of TiO<sub>2</sub>-NP, first

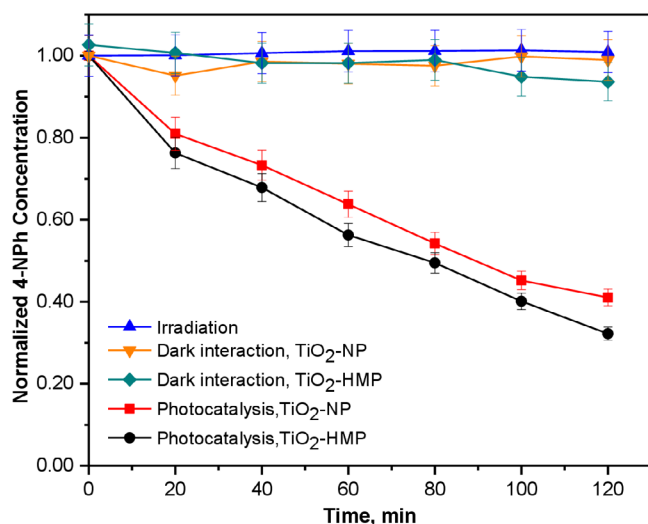


**FIGURE 15** Photocatalytic degradation profiles of 4-NPh using TiO<sub>2</sub> nanoparticle photocatalyst (TiO<sub>2</sub>-NP) and TiO<sub>2</sub> hierarchical microstructure photocatalyst (TiO<sub>2</sub>-HMP) specimens in comparison to sole irradiation and dark interactions.

order kinetic constants revealed an inconsistent trend in the range of  $k = 4.10 \times 10^{-3} \text{ min}^{-1}$  to  $7.14 \times 10^{-3} \text{ min}^{-1}$  with respect to increasing dose (0.1–0.5 g/100 ml). The reason of this inconsistency could be attributed to light harvesting capacities of both photocatalyst specimens as well as the 4-NPh.<sup>113</sup> Photocatalytic performance of TiO<sub>2</sub>-HMP was more consistent reflecting an increasing trend as  $k = 1.77 \times 10^{-3} \text{ min}^{-1}$  to  $8.22 \times 10^{-3} \text{ min}^{-1}$  in the range of 0.1–0.5 g/100 ml followed by a sharp decrease to  $k = 3.16 \times 10^{-3} \text{ min}^{-1}$  upon use of 0.6 g/100 ml. Respective kinetic model parameters as half-life ( $t_{1/2}$ , min) values and degradation rates ( $R \times 10^{-3}$ , mol/L min) were also presented in Table 1.

As expressed, prior to photocatalysis, preliminary experiments were performed referring to conditions (i) under irradiation in the absence of photocatalyst, and (ii) under dark in the sole presence of photocatalyst (Figure 15). No remarkable direct photodegradation of 4-NPh was noticed even upon prolonged irradiation periods the reason of which could be attributed to the very low quantum yields.<sup>114</sup> In non-irradiated conditions, an insignificant removal ( $\leq 5\%$ ) was attained most probably due to the minor adsorptive surface interactions between 4-NPh and TiO<sub>2</sub>-NP. In the presence of TiO<sub>2</sub>-HMP, a similar trend was also displayed both during the early stages of interaction and up to 80 min of exposure, followed by a slightly increasing trend. Under almost neutral pH experimental conditions, 4-NPh ( $pK_a = 7.15$ ) was present as both 4-nitrophenol/4-nitrophenolate anion. Based on the zeta potential measurements,  $pH_{zpc}$  of TiO<sub>2</sub>-HMP recorded as  $pH = 6.14$  expressing the presence of equally distributed positively and negatively charged surface sites. Due to the concomitantly acting electrostatic interactions, hydrogen bonding and/or van der Waals forces, the overall effect could be visualized as considerably lower adsorption extents prior to initiation of photocatalysis. It should also be indicated that under irradiation, photo-adsorption/desorption processes would also take place between the surface of the photocatalyst

specimen and the sole substrate, as well as the reaction intermediates and/or products. Upon photocatalytic treatment, a fast degradation of 4-NPh was observed irrespective of the type of the photocatalyst specimen. In the presence of TiO<sub>2</sub>-HMP, noticeably higher degradation efficiency as 64% of 4-NPh was recorded in 120 min as compared to 57% removal upon use of TiO<sub>2</sub>-NP. The enhanced photocatalytic activity of TiO<sub>2</sub>-HMP could be attributed to the different morphological characteristics compared to TiO<sub>2</sub>-NP. Higher surface area could usually supply more adsorption and active sites for photocatalytic reactions, favoring an increase in photocatalytic efficiency.<sup>112</sup> It could be concluded that self-doping was achieved during the preparation of TiO<sub>2</sub>-HMP and thus resulted in an enhancement of the photocatalytic degradation efficiency.

The effect of initial 4-NPh concentration on the degradation efficiency of TiO<sub>2</sub>-HMP (loading 0.5 g/100 ml) was investigated in the range of  $6.0 \times 10^{-5} \text{ mol/L}$  to  $1.2 \times 10^{-4} \text{ mol/L}$ . Degradation efficiencies expressed an inconsistent trend with respect to exposed irradiation of 100 min, followed by a concentration dependent decreasing profile upon 120 min. The respective kinetic constants were in the range of  $k = 1.24 \times 10^{-2} \text{ min}^{-1}$  to  $4.90 \times 10^{-3} \text{ min}^{-1}$ . The corresponding half-life variations were 56–141 min and the first order rates were  $R = 7.44 \times 10^{-3} \text{ mol/L min}$  to  $5.88 \times 10^{-3} \text{ mol/L min}$ . TiO<sub>2</sub>-HMP photocatalytic degradation rate of 4-NPh was inversely related to initial concentration under the specified experimental conditions. Since the 4-NP was chosen only as a model substrate, no analyses concerning the possible intermediates were performed.

## 4 | CONCLUSIONS

TiO<sub>2</sub>-NP and bio-inspired TiO<sub>2</sub>-HMP specimens were synthesized by a modified sol-gel method. RH was used as a biotemplate, preferentially excluding the disadvantages of chemical templates. A detailed characterization approach was directed to both RH and RHA to elucidate the baseline factors for understanding of the photocatalytic activities of TiO<sub>2</sub>-NP and TiO<sub>2</sub>-HMP, using 4-NPh as the model compound. TiO<sub>2</sub>-HMP exhibited a hierarchical mesoporous structure with lower crystallite size as verified by respective methods. Due to calcination of RH elements like S, N, Si and C were incorporated into the structure revealing in-situ self co-doped TiO<sub>2</sub>. The resultant effect was displayed by enhanced photocatalytic activity as evidenced by the degradation efficiency using 4-NPh as the substrate. The preparation methodology of TiO<sub>2</sub>-HMP could be improved as an advantage reducing the amount of TiO<sub>2</sub> at the same time increasing the beneficial use of an agricultural non-food waste. On the other hand, rather than using a commercial TiO<sub>2</sub>, two-step preparation methodology could be regarded as a minor disadvantage. In conclusion, using RH as a biotemplate to prepare a novel in-situ multidoped photocatalyst would not only reduce the environmental pressure but also could produce a value-added product for water treatment.

“The present article is dedicated to the memory of Prof. Dr. Zekiye Cinar, who passed away on July 22, 2021.”

## AUTHOR CONTRIBUTIONS

**Nazli Turkten:** Conceptualization (equal); investigation (equal); writing – original draft (equal); writing – review and editing (equal). **Betul Karatas:** Writing – review and editing (equal). **Yunus Karatas:** Writing – review and editing (equal). **Zekiye Cinar:** Conceptualization (equal); investigation (equal); writing – original draft (equal). **Miray Bekbolet:** Writing – original draft (equal); writing – review and editing (equal).

## DATA AVAILABILITY STATEMENT

The data that support the findings of this study are available from the corresponding author upon reasonable request.

## ORCID

Nazli Turkten  <https://orcid.org/0000-0001-9343-3697>

## REFERENCES

- Ollis DF, Pelizzetti E, Serpone N. Photocatalyzed destruction of water contaminants. *Environ Sci Technol*. 1991;25(9):1522-1529.
- Bahnemann DJC, Fox MA, Pelizzetti E, Pichat P, Serpone N. In: Helz GR, Zepp RG, Crosby DG, eds. *Aquatic and Surface Photochemistry*. Lewis Publishers; 1994.
- Pichat P. In: Ertl G, Knozinger H, Weitkamp J, eds. *Handbook of Heterogeneous Photo-Catalysis*. Vol 4. Wiley-VCH; 1997.
- Lazar MA, Varghese S, Nair SS. Photocatalytic water treatment by titanium dioxide: recent updates. *Catalysts*. 2012;2(4):572-601.
- Shaham-Waldmann N, Paz Y. Away from TiO<sub>2</sub>: a critical minireview on the developing of new photocatalysts for degradation of contaminants in water. *Mater Sci Semicond Process*. 2016;42:72-80.
- Gurkan Y, Kasapbasi E, Turkten N, Cinar Z. Influence of Se/N codoping on the structural, optical, electronic and photocatalytic properties of TiO<sub>2</sub>. *Molecules*. 2017;22(3):414.
- Turkten N, Cinar Z. Photocatalytic decolorization of azo dyes on TiO<sub>2</sub>: prediction of mechanism via conceptual DFT. *Catal Today*. 2017;287:169-175.
- Linsebigler AL, Lu G, Yates JT. Photocatalysis on TiO<sub>2</sub> surfaces: principles, mechanisms, and selected results. *Chem Rev*. 1995;95(3):735-758.
- Momeni MM. Study of synergistic effect among photo-, electro-, and sonoprocesses in photocatalyst degradation of phenol on tungsten-loaded titania nanotubes composite electrode. *Appl Phys A*. 2015;119(4):1413-1422.
- Momeni MM, Akbarinia M, Ghayeb Y. Preparation of S-W-codoped TiO<sub>2</sub> nanotubes and effect of various hole scavengers on their photoelectrochemical activity: alcohol series. *Int J Hydrogen Energy*. 2020;45(58):33552-33562.
- Sharifi T, Mohammadi T, Momeni MM, et al. Influence of photo-deposited Pt and Pd onto chromium doped TiO<sub>2</sub> nanotubes in photo-electrochemical water splitting for hydrogen generation. *Catalysts*. 2021;11(2):212.
- Gurkan YY, Turkten N, Hatipoglu A, Cinar Z. Photocatalytic degradation of cefazolin over N-doped TiO<sub>2</sub> under UV and sunlight irradiation: prediction of the reaction paths via conceptual DFT. *Chem Eng J*. 2012;184:113-124.
- Pelaez M, Nolan NT, Pillai SC, et al. A review on the visible light active titanium dioxide photocatalysts for environmental applications. *Appl Catal B*. 2012;125:331-349.
- Park H, Park Y, Kim W, Choi W. Surface modification of TiO<sub>2</sub> photocatalyst for environmental applications. *J Photochem Photobiol C: Photochem Rev*. 2013;15:1-20.
- Birben NC, Uyguner-Demirel CS, Sen-Kavurmaci S, et al. Comparative evaluation of anion doped photocatalysts on the mineralization and decolorization of natural organic matter. *Catal Today*. 2015;240(1):125-131.
- Birben NC, Uyguner-Demirel CS, Kavurmaci SS, et al. Application of Fe-doped TiO<sub>2</sub> specimens for the solar photocatalytic degradation of humic acid. *Catal Today*. 2017;281:78-84.
- Fang W, Xing M, Zhang J. Modifications on reduced titanium dioxide photocatalysts: a review. *J Photochem Photobiol C: Photochem Rev*. 2017;32:21-39.
- Byrne C, Subramanian G, Pillai SC. Recent advances in photocatalysis for environmental applications. *J Environ Chem Eng*. 2018;6(3):3531-3555.
- Turkten N, Cinar Z, Tomruk A, Bekbolet M. Copper-doped TiO<sub>2</sub> photocatalysts: application to drinking water by humic matter degradation. *Environ Sci Pollut Res Int*. 2019;26(36):36096-36106.
- Chiang L-F, Doong R. Cu-TiO<sub>2</sub> nanorods with enhanced ultraviolet and visible-light photoactivity for bisphenol a degradation. *J Hazard Mater*. 2014;277:84-92.
- Camposco R, Castillo S, Navarrete J, Gomez R. Synthesis, characterization and photocatalytic activity of TiO<sub>2</sub> nanostructures: nanotubes, nanofibers, nanowires and nanoparticles. *Catal Today*. 2016;266:90-101.
- Reddy PVG, Reddy BRP, Reddy MVK, et al. A review on multicomponent reactions catalysed by zero-dimensional/one-dimensional titanium dioxide (TiO<sub>2</sub>) nanomaterials: promising green methodologies in organic chemistry. *J Environ Manage*. 2020;111603:111603.
- Bai H, Liu Z, Lee SS, Sun DD. The effect of fabrication method of hierarchical 3D TiO<sub>2</sub> nanorod spheres on photocatalytic pollutants degradation. *Appl Catal, A*. 2012;447-448:193-199.
- Hu H, Qian D, Lin P, Ding Z, Cui C. Oxygen vacancies mediated in-situ growth of noble-metal (Ag, Au, Pt) nanoparticles on 3D TiO<sub>2</sub> hierarchical spheres for efficient photocatalytic hydrogen evolution from water splitting. *Int J Hydrogen Energy*. 2020;45(1):629-639.
- Ma X, Wang X, Yu C, et al. Effects of primary nanobuilding blocks on the photocatalytic performance of TiO<sub>2</sub> hierarchical hollow microspheres. *J Alloys Compd*. 2019;773:352-360.
- Bao Y, Guo R, Gao M, Kang Q, Ma J. Morphology control of 3D hierarchical urchin-like hollow SiO<sub>2</sub>@TiO<sub>2</sub> spheres for photocatalytic degradation: influence of calcination temperature. *J Alloys Compd*. 2021;853:157202.
- Kamata K, Lu Y, Xia Y. Synthesis and characterization of monodispersed core-shell spherical colloids with movable cores. *J Am Chem Soc*. 2003;125(9):2384-2385.
- Dun H, Zhang W, Wei Y, Xiuqing S, Li Y, Chen L. Layer-by-layer self-assembly of multilayer zirconia nanoparticles on silica spheres for HPLC packings. *Anal Chem*. 2004;76(17):5016-5023.
- Jiao Y, Peng C, Guo F, et al. Facile synthesis and photocatalysis of size-distributed TiO<sub>2</sub> hollow spheres consisting of {116} plane-oriented nanocrystallites. *J Phys Chem C*. 2011;115(14):6405-6409.
- Leshuk T, Linley S, Baxter G, Gu F. Mesoporous hollow sphere titanium dioxide photocatalysts through hydrothermal silica etching. *ACS App Mater Interfaces*. 2012;4(11):6062-6070.
- Nakata K, Fujishima A. TiO<sub>2</sub> photocatalysis: design and applications. *J Photochem Photobiol C: Photochem Rev*. 2012;13(3):169-189.
- Wang X, Feng J, Bai Y, Zhang Q, Yin Y. Synthesis, properties, and applications of hollow micro-/nanostructures. *Chem Rev*. 2016;116(18):10983-11060.
- Mozaffari N, Mohammadi MR, Garmaroudi ZA, Gharavi PSM. Comparative study on effect of titania morphology for light harvesting and scattering of DSSCs: mesoporous nanoparticles, microspheres, and dandelion-like particles. *Environ Prog Sustain Energy*. 2016;35(6):1818-1826.
- Li X, Yu J, Jaroniec M. Hierarchical photocatalysts. *Chem Soc Rev*. 2016;45(9):2603-2636.
- Caruso F, Shi X, Caruso RA, Susa A. Hollow Titania spheres from layered precursor deposition on sacrificial colloidal core particles. *Adv Mater*. 2001;13(10):740-744.
- Ye M, Chen Z, Wang W, Shen J, Ma J. Hydrothermal synthesis of TiO<sub>2</sub> hollow microspheres for the photocatalytic degradation of 4-chloronitrobenzene. *J Hazard Mater*. 2010;184(1-3):612-619.

37. Zeng Y, Wang X, Wang H, Dong Y, Ma Y, Yao J. Multi-shelled titania hollow spheres fabricated by a hard template strategy: enhanced photocatalytic activity. *Chem Commun.* 2010;46(24):4312-4314.
38. Hu J, Chen M, Fang X, Wu L. Fabrication and application of inorganic hollow spheres. *Chem Soc Rev.* 2011;40(11):5472-5491.
39. Zhao W, Feng L, Yang R, Zheng J, Li X. Synthesis, characterization, and photocatalytic properties of Ag modified hollow  $\text{SiO}_2/\text{TiO}_2$  hybrid microspheres. *Appl Catal B.* 2011;103(1-2):181-189.
40. Shi X, Pan L, Chen S, et al. Zn(II)-PEG 300 globules as soft template for the synthesis of hexagonal ZnO microns by the hydrothermal reaction method. *Langmuir.* 2009;25(10):5940-5948.
41. Réthoré G, Pandit A. Use of templates to fabricate nanoscale spherical structures for defined architectural control. *Small.* 2010;6(4):488-498.
42. Liu Y, Goebel J, Yin Y. Templated synthesis of nanostructured materials. *Chem Soc Rev.* 2013;42(7):2610-2653.
43. Dou L, Gao L, Yang X, Song X. Hierarchical architectures  $\text{TiO}_2$ : pollen-induced synthesis, remarkable crystalline-phase stability, tunable size, and reused photo-catalysis. *J Hazard Mater.* 2012;203-204:363-369.
44. Bu D, Zhuang H. Biotemplated synthesis of high specific surface area copper-doped hollow spherical titania and its photocatalytic research for degrading chlorotetracycline. *Appl Surf Sci.* 2013;265:677-685.
45. He Z, Que W, He Y. Synthesis and characterization of bioinspired hierarchical mesoporous  $\text{TiO}_2$  photocatalysts. *Mater Lett.* 2013;94:136-139.
46. He T, Weng Y, Yu P, et al. Bio-template mediated in situ phosphate transfer to hierarchically porous  $\text{TiO}_2$  with localized phosphate distribution and enhanced photoactivities. *J Phys Chem C.* 2014;118(9):4607-4617.
47. Li J, Shi J, Li Y, Ding Z, Huang J. A biotemplated synthesized hierarchical Sn-doped  $\text{TiO}_2$  with superior photocatalytic capacity under simulated solar light. *Ceram Int.* 2021;47(6):8218-8227.
48. Shu-Juan B, Chao L, Mao-Wen X, Chang-Jun C, Dian-Zeng J. Environment-friendly biomimetic synthesis of  $\text{TiO}_2$  nanomaterials for photocatalytic application. *Nanotechnology.* 2012;23(20):205601.
49. Chen Y, Wang C, Bai B, Yang L. Fabrication of  $\text{TiO}_2$  hollow spheres using yeast as bio-templates and their photocatalytic performance for the degradation of CBW wastewater. Paper presented at 4th International Conference on Bioinformatics and Biomedical Engineering; 2010:1-4.
50. Tang LQ, Ni W, Zhao H, Xu Q, Jiao JX. Preparation of macroporous  $\text{TiO}_2$  by starch microspheres template with assistance of supercritical  $\text{CO}_2$ . *Bioresources.* 2008;4(1):11-38.
51. Royston ES, Brown AD, Harris MT, Culver JN. Preparation of silica stabilized tobacco mosaic virus templates for the production of metal and layered nanoparticles. *J Colloid Interface Sci.* 2009;332(2):402-407.
52. Li X, Fan T, Zhou H, et al. Enhanced light-harvesting and photocatalytic properties in morph- $\text{TiO}_2$  from green-leaf biotemplates. *Adv Funct Mater.* 2009;19(1):45-56.
53. Shenmin Z, Di Z, Zhixin C, et al. A simple and effective approach towards biomimetic replication of photonic structures from butterfly wings. *Nanotechnology.* 2009;20(31):315303.
54. Yu Y, Piao L, Xia J, et al. A facile one-pot synthesis of N-La codoped  $\text{TiO}_2$  porous materials with bio-hierarchical architectures and enhanced photocatalytic activity. *Mater Chem Phys.* 2016;182:77-85.
55. Song N, Jiang H, Cui T, Chang L, Wang X. Synthesis and enhanced gas-sensing properties of mesoporous hierarchical  $\alpha\text{-Fe}_2\text{O}_3$  architectures from an eggshell membrane. *Micro Nano Lett.* 2012;7(9):943-946.
56. Chungsangunsit T, Gheewala SH, Patumsawad S. Environmental assessment of electricity production from rice husk: a case study in Thailand. *Int Energy J.* 2005;6(1):3-47.
57. Chen H, Zhao L, Xiang Y, et al. A novel Zn- $\text{TiO}_2/\text{C}/\text{SiO}_2$  nanoporous material on rice husk for photocatalytic applications under visible light. *Desalin Water Treat.* 2016;57(21):9660-9670.
58. Zhaohui H, Hui C, Lei Z, et al. Biogenic hierarchical MIL-125/ $\text{TiO}_2$ @- $\text{SiO}_2$  derived from rice husk and enhanced photocatalytic properties for dye degradation. *Photochem Photobiol.* 2018;94(3):512-520.
59. de Cordoba MCF, Matos J, Montaña R, et al. Sunlight photoactivity of rice husks-derived biogenic silica. *Catal Today.* 2019;328:125-135.
60. Wang W, Chen H, Fang J, Lai M. Large-scale preparation of rice-husk-derived mesoporous  $\text{SiO}_2$ @ $\text{TiO}_2$  as efficient and promising photocatalysts for organic contaminants degradation. *Appl Surf Sci.* 2019;467-468:1187-1194.
61. Adam F, Appaturi JN, Khanam Z, Thankappan R, Nawi MAM. Utilization of tin and titanium incorporated rice husk silica nanocomposite as photocatalyst and adsorbent for the removal of methylene blue in aqueous medium. *Appl Surf Sci.* 2013;264:718-726.
62. Hui C, Lei Z, Xitang W, Shujing L, Zhongxing L. Preparation of nanoporous  $\text{TiO}_2/\text{SiO}_2$  composite with rice husk as template and its photocatalytic property. *Rare Met Mater Eng.* 2015;44(7):1607-1611.
63. Artkla S, Kim W, Choi W, Wittayakun J. Highly enhanced photocatalytic degradation of tetramethylammonium on the hybrid catalyst of titania and MCM-41 obtained from rice husk silica. *Appl Catal B.* 2009;91(1):157-164.
64. Yener HB, Helvacı ŞŞ. Effect of synthesis temperature on the structural properties and photocatalytic activity of  $\text{TiO}_2/\text{SiO}_2$  composites synthesized using rice husk ash as a  $\text{SiO}_2$  source. *Sep Purif Technol.* 2015;140:84-93.
65. Klankaw P, Chawengkijwanich C, Grisdanurak N, Chiarakorn S. The hybrid photocatalyst of  $\text{TiO}_2$ - $\text{SiO}_2$  thin film prepared from rice husk silica. *Superlattices Microstruct.* 2012;51(3):343-352.
66. da Silva WL, Hamilton JWW, Sharma PK, Dunlop PSM, Byrne JA, dos Santos JHZ. Agro and industrial residues: potential raw materials for photocatalyst development. *J Photochem Photobiol A.* 2021;411:113184.
67. Goodman BA. Utilization of waste straw and husks from rice production: a review. *J Bioresour Bioprod.* 2020;5(3):143-162.
68. Calvert JG, Pitts JN. *Photochemistry.* Wiley; 1966:783-786.
69. Chandrasekhar S, Satyanarayana KG, Pramada PN, Raghavan P, Gupta TN. Review processing, properties and applications of reactive silica from rice husk—an overview. *J Mater Sci.* 2003;38(15):3159-3168.
70. Daifullah AAM, Girgis BS, Gad HMH. Utilization of agro-residues (rice husk) in small waste water treatment plans. *Mater Lett.* 2003;57(11):1723-1731.
71. Genieva SD, Turmanova SC, Dimitrova AS, Vlaev LT. Characterization of rice husks and the products of its thermal degradation in air or nitrogen atmosphere. *J Therm Anal Calorim.* 2008;93(2):387-396.
72. Weldekidan H, Strezov V, Town G, Kan T. Production and analysis of fuels and chemicals obtained from rice husk pyrolysis with concentrated solar radiation. *Fuel.* 2018;233:396-403.
73. Diaz AB, Moretti MM, Bezerra-Bussoli C, et al. Evaluation of microwave-assisted pretreatment of lignocellulosic biomass immersed in alkaline glycerol for fermentable sugars production. *Bioresour Technol.* 2015;185:316-323.
74. Daffalla SB, Mukhtar H, Shaharun MS. Characterization of adsorbent developed from rice husk: effect of surface functional group on phenol adsorption. *J Appl Sci.* 2010;10:1060-1067.
75. Socrates G. Infrared characteristic group frequencies, Tables and charts. 3rd (Eds.); 2004:366.
76. Markovska IG, Lyubchev LA. A study on the thermal destruction of rice husk in air and nitrogen atmosphere. *J Therm Anal Calorim.* 2007;89(3):809-814.
77. Chandrasekhar S, Pramada PN. Rice husk ash as an adsorbent for methylene blue—effect of ashing temperature. *Adsorption.* 2006;12(1):27-43.



78. James J, Rao MS. Silica from rice husk through thermal decomposition. *Thermochim Acta*. 1986;97:329-336.
79. Alvarez VA, Vázquez A. Thermal degradation of cellulose derivatives/starch blends and sisal fibre biocomposites. *Polym Degrad Stab*. 2004;84(1):13-21.
80. Carmona VB, Oliveira RM, Silva WTL, Mattoso LHC, Marconcini JM. Nanosilica from rice husk: extraction and characterization. *Ind Crops Prod*. 2013;43:291-296.
81. Shaheen SM, Antoniadis V, Shahid M, et al. Sustainable applications of rice feedstock in agro-environmental and construction sectors: a global perspective. *Renew Sustain Energy Rev*. 2022;153:111791.
82. Angelito-Bañós J, Avilés-Arellano LMR, Barreiro-Rodríguez G, et al. Structural characterization of silver doped silica prepared by two different wet chemical methods. *J Sol-Gel Sci Technol*. 2004;30(2):89-94.
83. Wazir AH, Wazir IU, Wazir AM. *Preparation and Characterization of Rice Husk Based Physical Activated Carbon*. Recovery Util Environ Eff; 2020:1-11.
84. Yuzer N, Cinar Z, Aköz F, et al. Influence of raw rice husk addition on structure and properties of concrete. *Construct Build Mater*. 2013;44:54-62.
85. Yurdakal S, Garlisi C, Özcan L, Bellardita M, Palmisano G. Chapter 4 - (photo) catalyst characterization techniques: adsorption isotherms and BET, SEM, FTIR, UV-vis, photoluminescence, and electrochemical characterizations. In: Marci G, Palmisano L, eds. *Heterogeneous Photocatalysis*. Elsevier; 2019:87-152.
86. Spurr RA, Myers H. Quantitative analysis of anatase-rutile mixtures with an X-ray diffractometer. *Anal Chem*. 1957;29(5):760-762.
87. Zhang H, Banfield JF. Understanding polymorphic phase transformation behavior during growth of nanocrystalline aggregates: insights from TiO<sub>2</sub>. *J Phys Chem B*. 2000;104(15):3481-3487.
88. Ohtani B, Prieto-Mahaney OO, Li D, Abe R. What is Degussa (Evonik) P25? Crystalline composition analysis, reconstruction from isolated pure particles and photocatalytic activity test. *J Photochem Photobiol A*. 2010;216(2):179-182.
89. Scherrer P. Estimation of the size and internal structure of colloidal particles by means of röntgen. *Nachrichten von der Gesellschaft der Wissenschaften Zu Göttingen*. 1918;2:96-100.
90. Yalçın Y, Kılıç M, Çınar Z. Fe<sup>+3</sup>-doped TiO<sub>2</sub>: a combined experimental and computational approach to the evaluation of visible light activity. *Appl Catal B*. 2010;99(3-4):469-477.
91. Hu C, Duo S, Zhang R, Li M, Xiang J, Li W. Nanocrystalline anatase TiO<sub>2</sub> prepared via a facile low temperature route. *Mater Lett*. 2010; 64(19):2040-2042.
92. Bessergenev VG, Mateus MC, Botelho do Rego AM, Hantusch M, Burkel E. An improvement of photocatalytic activity of TiO<sub>2</sub> Degussa P25 powder. *Appl Catal A*. 2015;500:40-50.
93. Xu Y-h, Zeng Z-x. The preparation, characterization, and photocatalytic activities of Ce-TiO<sub>2</sub>/SiO<sub>2</sub>. *J Mol Catal A: Chem*. 2008;279(1): 77-81.
94. Zhang M, Meng F, Zhang S, Zeng Y, Zhong Q. Sulfur-doping promoting peroxone reaction over TiO<sub>2</sub> for highly effective NO oxidation at low temperature: experimental and DFT studies. *Chem Eng J*. 2022; 429:132475.
95. Wu D, Zhang C, Zhang Z, Zhu H. In situ doping of carbon and sulfur from multifunctional agents to TiO<sub>2</sub> nanospheres in water-acetone mixed solvent. *Mater Res Bull*. 2012;47(11):3427-3431.
96. Zhou L, Cai M, Zhang X, Cui N, Chen G, Zou G-y. In-situ nitrogen-doped black TiO<sub>2</sub> with enhanced visible-light-driven photocatalytic inactivation of *Microcystis aeruginosa* cells: synthesis, performance and mechanism. *Appl Catal B*. 2020;272:119019.
97. Nguyen-Le M-T, Lee B-K. High temperature synthesis of interfacial functionalized carboxylate mesoporous TiO<sub>2</sub> for effective adsorption of cationic dyes. *Chem Eng J*. 2015;281:20-33.
98. Yuan W, Cheng L, An Y, et al. Laminated hybrid junction of sulfur-doped TiO<sub>2</sub> and a carbon substrate derived from Ti<sub>3</sub>C<sub>2</sub> MXenes: toward highly visible light-driven photocatalytic hydrogen evolution. *Adv Sci*. 2018;5(6):1700870.
99. Reddy BM, Ganesh I, Reddy EP. Study of dispersion and thermal stability of V<sub>2</sub>O<sub>5</sub>/TiO<sub>2</sub>-SiO<sub>2</sub> catalysts by XPS and other techniques. *J Phys Chem B*. 1997;101(10):1769-1774.
100. Piątkowska A, Janus M, Szymański K, Mozia S. C-, N- and S-doped TiO<sub>2</sub> photocatalysts: a review. *Catalysts*. 2021;11(1):144.
101. Kubelka P, Munk FA. Contribution to the optics of pigments. *Z Tech Phys*. 1931;12:593-599.
102. Hamrouni A, Azzouzi H, Rayes A, Palmisano L, Ceccato R, Parrino F. Enhanced solar light photocatalytic activity of Ag doped TiO<sub>2</sub>-Ag<sub>3</sub>PO<sub>4</sub> composites. *Nanomaterials*. 2020;10(4):795.
103. Yang Z-Y, Shen G-Y, He Y-P, Liu X-X, Yang S-J. Preparation of TiO<sub>2</sub>/SiO<sub>2</sub> composite oxide and its photocatalytic degradation of rhodamine B. *J Porous Mater*. 2016;23(3):589-599.
104. Yaparatne S, Tripp CP, Amirbahman A. Photodegradation of taste and odor compounds in water in the presence of immobilized TiO<sub>2</sub>-SiO<sub>2</sub> photocatalysts. *J Hazard Mater*. 2018;346:208-217.
105. Hu Y, Li C, Gu F, Zhao Y. Facile flame synthesis and photoluminescent properties of core/shell TiO<sub>2</sub>/SiO<sub>2</sub> nanoparticles. *J Alloys Compd*. 2007;432(1):L5-L9.
106. Ramakrishnan VM, Natarajan M, Santhanam A, Asokan V, Velauthapillai D. Size controlled synthesis of TiO<sub>2</sub> nanoparticles by modified solvothermal method towards effective photo catalytic and photovoltaic applications. *Mater Res Bull*. 2018;97:351-360.
107. Choudhury B, Choudhury A. Oxygen vacancy and dopant concentration dependent magnetic properties of Mn doped TiO<sub>2</sub> nanoparticle. *Curr Appl Phys*. 2013;13(6):1025-1031.
108. Lei XF, Xue XX, Yang H, et al. Effect of calcination temperature on the structure and visible-light photocatalytic activities of (N, S and C) co-doped TiO<sub>2</sub> nano-materials. *Appl Surf Sci*. 2015;332:172-180.
109. Kadam AN, Salunkhe TT, Kim H, Lee S-W. Biogenic synthesis of mesoporous N-S-C tri-doped TiO<sub>2</sub> photocatalyst via ultrasonic-assisted derivatization of biotemplate from expired egg white protein. *Appl Surf Sci*. 2020;518:146194.
110. Sing KSW. Reporting physisorption data for gas/solid systems with special reference to the determination of surface area and porosity (recommendations 1984). *Pure Appl Chem*. 1985;57(4):603-619.
111. Hu J-L, Qian H-S, Li J-J, Hu Y, Li Z-Q, Yu S-H. Synthesis of mesoporous SiO<sub>2</sub>@TiO<sub>2</sub> core/shell nanospheres with enhanced photocatalytic properties. *Part Part Syst Charact*. 2013;30(4):306-310.
112. Yan Z, He J, Guo L, et al. Biotemplated mesoporous TiO<sub>2</sub>/SiO<sub>2</sub> composite derived from aquatic plant leaves for efficient dye degradation. *Catalysts*. 2017;7(3):82.
113. Egerton TA, Christensen PA, Harrison RW, Wang JW. The effect of UV absorption on the photocatalytic oxidation of 2-nitrophenol and 4-nitrophenol. *J Appl Electrochem*. 2005;35(7):799-813.
114. Di Paola A, Augugliaro V, Palmisano L, Pantaleo G, Savinov E. Heterogeneous photocatalytic degradation of nitrophenols. *J Photochem Photobiol A*. 2003;155(1):207-214.

## SUPPORTING INFORMATION

Additional supporting information can be found online in the Supporting Information section at the end of this article.

**How to cite this article:** Turkten N, Karatas B, Karatas Y, Cinar Z, Bekbolet M. A facile synthesis of bio-inspired hierarchical microstructure TiO<sub>2</sub>: Characterization and photocatalytic activity. *Environ Prog Sustainable Energy*. 2022; e14054. doi:10.1002/ep.14054